Engineering Analysis with Boundary Elements 135 (2022) 182–195

Contents lists available at ScienceDirect

Engineering Analysis with Boundary Elements

journal homepage: www.elsevier.com/locate/enganabound

Bi-material topology optimization for fully coupled structural-acoustic systems with isogeometric FEM–BEM

L.L. Chen [a,b,c,d], H. Lian [a,b,e,*], Z. Liu [f], Y. Gong [g], C.J. Zheng [h], S.P.A. Bordas [e,i]

[a] Henan International Joint Laboratory of Structural Mechanics and Computational Simulation, Huanghuai University, Zhumadian 463003, Henan, China
[b] Key Laboratory of In-situ Property-improving Mining of Ministry of Education, Taiyuan University of Technology, Taiyuan, Shanxi, China
[c] School of Architectural Engineering, Huanghuai University, Zhumadian 463003, Henan, China
[d] College of Architecture and Civil Engineering, Xinyang Normal University, China
[e] Institute for Computational Engineering, Faculty of Science, Technology and Communication, University of Luxembourg, Luxembourg
[f] Glasgow Computational Engineering Centre, University of Glasgow, G12 8LT, Glasgow, UK
[g] Institute of Electronics Packaging Technology and Reliability, Faculty of Materials and Manufacturing, Beijing University of Technology, Beijing, 100124, China
[h] Institute of Sound and Vibration Research, Hefei University of Technology, China
[i] School of Engineering, Cardiff University, The Parade, CF24 3AA, Cardiff, UK

ARTICLE INFO

Keywords:
Topology optimization
Subdivision surfaces
Isogeometric analysis
Structural Acoustics
FEM
BEM

ABSTRACT

This paper presents a novel method for topology optimization of vibrating structures interacted with acoustic wave for the purpose of minimizing radiated sound power level. We consider exterior acoustic fields and bi-material shell models without damping in this work. Within the isogeometric analysis framework, we employ Catmull–Clark subdivision surfaces to construct geometries and discretize physical fields. The isogeometric finite element method with Kirchhoff–Love shell elements is coupled with the isogeometric boundary element method in acoustics. The topology optimization is performed through density-based approaches, in which the sensitivities are evaluated with adjoint variable methods. Numerical experiments demonstrate the validity and effectiveness of the algorithm for topology optimization of structural-acoustic interaction systems.

1. Introduction

Noise control is an important issue in a wide range of engineering fields. Substantial efforts have been made in structural design for the purpose of bringing down noise levels. However, traditional design methods heavily rely on trial-and-error procedures, which require significant human intervention with no guarantee of satisfactory results. As a pace-setting technology, topology optimization is deemed an effective technique to find the optimal material distribution automatically in large design spaces [1–4]. There exist a variety of topology optimization algorithms such as the density-based method, the Level Set Method [5–7], the Moving Morphable Component method [8,9], and the Deformable Simplicial Complex method [10–12]. Among them, the density-based method achieves widespread popularity due to its computational efficiency and ease of implementation, although the appearance of intermediary materials poses challenges for some applications. Dühring et al. [13] applied density-based method to optimize of the layout of sound absorbing materials and topology of sound barriers. Christiansen et al. [10] adopted density-based approach for geometrically robust design of acoustic cavity and validated the optimized result with laboratory experiments [14].

Topology optimization is commonly used with the Finite Element Method (FEM) for its versatility, but FEM has inherent difficulty in dealing with infinite acoustic domains exterior to structural surfaces. In FEM, unbounded domains need to be truncated via fictitious boundary surfaces, and Sommerfeld radiation conditions are approximated by resorting to special techniques. In comparison, the Boundary Element Method (BEM) seems to be more appealing in exterior acoustics problems, since it only discretizes the inner boundary of the acoustic domain (i.e. the structural surfaces), meanwhile fulfilling the boundary conditions at infinity automatically [15–23]. It is highlighted that the advantage of BEM in dimension reduction not only decreases degrees of freedom, but more importantly, facilitates preprocessing significantly.

An acoustic wave propagating in the fluid may excite the vibration of structures, which radiates and reflects an additional acoustic wave to the fluid. Such strong structural-acoustic interaction phenomenon is particularly manifest when thin-walled structures are involved. To conduct numerical simulation and topology optimization for structural-acoustic interaction systems, coupling FEM and BEM offers the benefits

* Corresponding author at: Key Laboratory of In-situ Property-improving Mining of Ministry of Education, Taiyuan University of Technology, Taiyuan, Shanxi, China.
E-mail address: lianhaojie@tyut.edu.cn (H. Lian).

https://doi.org/10.1016/j.enganabound.2021.11.005
Received 26 May 2021; Received in revised form 1 September 2021; Accepted 4 November 2021
Available online 4 December 2021

of fully exploiting their advantages in structural dynamics and exterior acoustic problems, respectively [24–26]. Everstine and Henderson firstly coupled the FEM–BEM for vibration-acoustic analysis [27], which is further accelerated by introducing fast multipole methods [28,29] for large scale problems.

The classical numerical methods based on Lagrange polynomial basis functions rely on polygonal meshes to represent geometries, which possesses several shortcomings. Firstly, meshing is a laborious and time-consuming process [30,31]. Secondly, it degrades the analysis accuracy of structural-acoustic interaction problems as they are highly sensitive to geometric imperfection. Thirdly, the C_0 continuity across Lagrangian elements inhibits the wide use of Kirchhoff–Love theory, despite its well-recognized advantages in thin-shell analysis. The isogeometric analysis (IGA) proposed by Hughes et al. provides a promising tool to overcome these deficiencies [32]. The core idea of the IGA is to employ basis functions of Computer-Aided Design (CAD) to discretize physical fields whereby the geometric accuracy and high order continuity are achieved. In addition, the property of IGA in integrating numerical analysis and CAD makes it amenable to structural optimization. IGA was initially used in the framework of FEM based on Non-Uniform rational B-splines (NURBS), and later on was extended to BEM [33,34] and incorporated various CAD modeling techniques including trimmed NURBS [35,36], T-splines [37], Subdivision surfaces [38–40], etc. Isogeometric FEM shows superior performance in Kirchhoff–Love shell theory, [38], and isogeometric BEM achieved enormous success in acoustics [41]. Zhao. et al. carried out structural-acoustic interaction analysis by coupling isogeometric FEM and BEM [42]. Yang et al. combined the collocation-based isogeometric BEM and the isogeometric Reissner–Mindlin shell elements to conduct the mixed dimensional solid-shell coupling analysis [43]. Chen et al. conducted topology optimization in acoustics using isogeometric BEM without taking into account the impact of structural vibration [16]. Shape optimization in acoustic using isogeometric BEM are presented in [44–46].

In this work, we conduct topology optimization for bi-material structures without damping. The structural-acoustic interaction effect is taken into account by coupling the isogeometric FEM/BEM. The geometric models are constructed with Catmull–Clark subdivision surfaces, which are selected mainly for the ability of generating water-tight geometries with bounded curvature. The basis functions in subdivision surfaces are employed to discretize the weak form formulated in shell vibration analysis and the boundary integral form of Helmholtz equations. The remainder of the paper is organized as follows. In Section 2, the fundamental concepts of Catmull–Clark subdivision surfaces are introduced. Section 3 formulates the governing equations of coupled isogeometric FEM–BEM for structural-acoustic interaction. Section 4 is devoted to the formulation of density-based topology optimization. Section 5 presents numerical examples of acoustic topology optimization, followed by the conclusion section.

2. Catmull–Clark subdivision surfaces

Catmull and Clark [47] proposed an algorithm which repeatedly subdivide an initial quadrilateral grid to produce a smooth surface. This technique was widely used in animation industries since later 1970s. The Catmull–Clark subdivision surface can be considered as a tensor-product of two curves generated using Lane–Riesenfeld subdivision algorithm. The Lane–Riesenfeld subdivision algorithm successively refines a curve starting from an initial control polygon. After a number of subdivisions, the limiting curve of Lane–Riesenfeld subdivision algorithm is identical to a cubic B-spline.

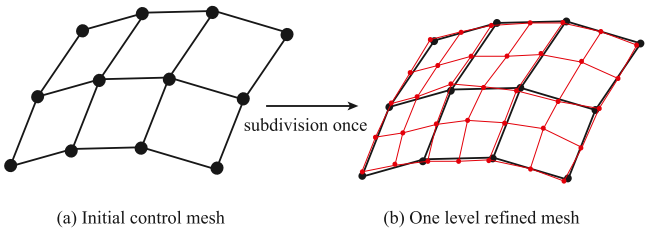

Fig. 1. Catmull–Clark subdivision algorithm for surfaces. The black points indicate the control points before the subdivision, and the red points indicate the control points after the subdivision. (For interpretation of the references to color in this figure legend, the reader is referred to the web version of this article.)

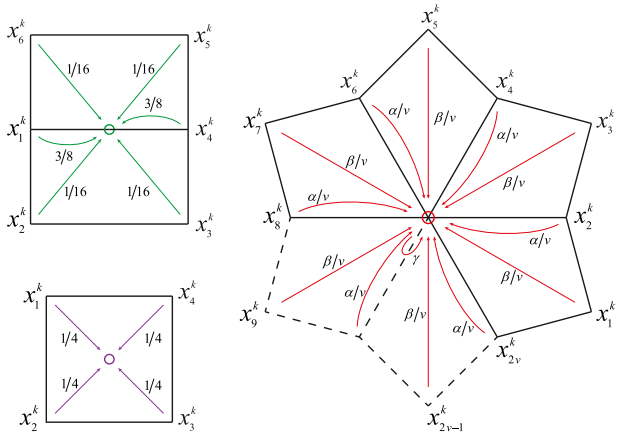

Fig. 2. The topology scheme of Catmull–Clark subdivision surface. The green circle dot is the vertex inserted in the middle of an edge, the purple circle the vertex inserted in the middle of an element, and the red circle dot the vertex formed by the transfer of a vertex in a parent element. (For interpretation of the references to color in this figure legend, the reader is referred to the web version of this article.)

2.1. Rules of Catmull–Clark subdivision

The first step for a designer to build geometries with Catmull–Clark subdivision surfaces is constructing a control grid, which is a polygon mesh with quadrilateral elements whose vertices are called control points or control vertices. Afterwards, the control grid is subdivided in which process new control points are introduced and the positions of the existing control points are updated, as illustrated in Fig. 1. The control grid can be subdivided repeatedly, and the subdivision process from the subdivision level k to the level $k+1$ follows the following rule (Fig. 2).

- Suppose the two vertices of the inner edge are $\mathbf{P}_1^k$ and $\mathbf{P}_4^k$, and the vertices of the two elements sharing this edge are $\mathbf{P}_2^k$, $\mathbf{P}_3^k$, $\mathbf{P}_5^k$ and $\mathbf{P}_6^k$, respectively. Then the new edge point $\mathbf{P}^{k+1}$ generated by this inner edge is

$$\mathbf{P}^{k+1} = \frac{3}{8}(\mathbf{P}_1^k + \mathbf{P}_2^k) + \frac{1}{16}(\mathbf{P}_3^k + \mathbf{P}_4^k + \mathbf{P}_5^k + \mathbf{P}_6^k) \tag{1}$$

- For an element with the four vertices of $\mathbf{P}_1^k$, $\mathbf{P}_2^k$, $\mathbf{P}_3^k$ and $\mathbf{P}_4^k$, the newly inserted point $\mathbf{P}^{k+1}$ inside the element is

$$\mathbf{P}^{k+1} = \frac{1}{4}(\mathbf{P}_1^k + \mathbf{P}_2^k + \mathbf{P}_3^k + \mathbf{P}_4^k) \tag{2}$$

- For an internal vertex $\mathbf{P}^k$, we denote its one-neighbor vertices by $\mathbf{P}_i^k (i = 1, 2, \ldots, 2v)$, in which the vertices with odd subscripts are directly connected to $\mathbf{P}^k$, and the ones with even subscripts are on the diagonal line of quadrilateral element. Correspondingly, the updated position of the vertex is

$$\mathbf{P}^{k+1} = \frac{\alpha}{v}\sum_{i=1}^{v}\mathbf{P}_{2i-1}^k + \frac{\beta}{v}\sum_{i=1}^{v}\mathbf{P}_{2i}^k + \gamma\mathbf{P}^k \tag{3}$$

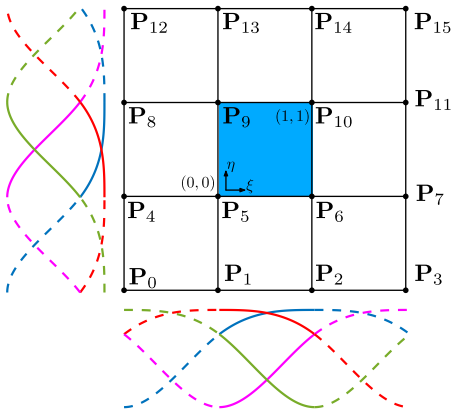

Fig. 3. Element patches for evaluating a Catmull–Clark subdivision element. (For interpretation of the references to color in this figure legend, the reader is referred to the web version of this article.)

where $\alpha = \frac{3}{2v}$, $\beta = \frac{1}{4v}$, $\gamma = 1 - \alpha - \beta$.

The subdivision can be repeated recursively in this way until the ultimate convergent mesh is obtained.

2.2. Evaluate a regular element

A Catmull–Clark subdivision surface element is called regular element if all of its vertices have valences of 4, for example, the colored element shown in Fig. 3. Evaluation of a point in the regular element requires to form an element patch that is defined as a set containing all the elements which share vertices with the target element. A regular element patch has 9 elements with 16 vertices. A surface point with parametric coordinates (ξ, η) can be evaluated by interpolating these control points with 16 basis functions as

$$\mathbf{x}(\xi,\eta) = \sum_{a=0}^{15} N_a(\xi,\eta)\mathbf{P}_a \tag{4}$$

where $\mathbf{x}$ indicates the Cartesian coordinates of the point, $\mathbf{P}_a$ the control points, and N_a are basis functions that are defined as

$$N_a(\xi,\eta) = N_{a\%4}(\xi)N_{\lfloor a/4 \rfloor}(\eta),\ a = 0, 1, \ldots, 15 \tag{5}$$

and $N(\xi)$ or $N(\eta)$ are cubic B-splines defined as

$$\begin{aligned} N_1(\xi) &= \frac{1}{6}[1 - 3\xi + 3\xi^2 - \xi^3], & N_2(\xi) &= \frac{1}{6}[4 - 6\xi^2 + 3\xi^3], \\ N_3(\xi) &= \frac{1}{6}[1 + 3\xi + 3\xi^2 - 3\xi^3], & N_4(\xi) &= \frac{1}{6}\xi^3 \end{aligned} \tag{6}$$

where % denotes the remainder operator which gives the remainder of the integer division. They are presented in Fig. 3.

2.3. Evaluate an element with an extraordinary vertex

A vertice with the valence not equal to 4 is called extraordinary vertice, and an element containing at least one extraordinary vertice is irregular. A favorable feature of subdivision surfaces compared to other competitors in CAD is that it is able to handle extraordinary vertices by guaranteeing bounded curvature at them. Suppose we want to evaluate the Cartesian coordinate of a target point with the parametric coordinate (ξ, η) which is located in an element containing one extraordinary vertex at the lower-left corner (Fig. 4(a)). $\mathbb{P}_0$ denotes the set collecting the control points of the patch corresponding to this irregular element,

$$\mathbb{P}_0 = \{\mathbf{P}_0, \mathbf{P}_1, \ldots, \mathbf{P}_{2\kappa+6}, \mathbf{P}_{2\kappa+7}\} \tag{7}$$

where κ is the valence of the extraordinary vertex and $\mathbb{P}_0$ contains $2\kappa+8$ vertices (Fig. 4(a)).

We divide the irregular element into four sub-elements through a subdivision. Among them three sub-elements are regular and one still has an extraordinary point (Fig. 4(b)). If the target point is located in the irregular sub-element, the sub-element will be subdivided repeatedly until the target point falls into a regular sub-element. We use $\Omega_{n,k}$ to denote the sub-element, in which the subscript n indicates the subdivision level and k the sub-element index that takes the value from 1 to 4. The indices of the sub-elements are numerated such that $\Omega_{n,1}$, $\Omega_{n,2}$ and $\Omega_{n,3}$ stand for regular elements, and $\Omega_{n,4}$ the irregular element. See Fig. 4(c). The maximum subdivision level can be determined as

$$n = \lfloor \min\left(-\log_2(\xi), -\log_2(\eta)\right) + 1 \rfloor \tag{8}$$

After the subdivision, the control points of the patch are also changed (Fig. 4(b)). We use $\mathbb{P}_n$ to denote the control point set corresponding to the patch of the irregular element after nth refinement. The control points in $\mathbb{P}_n$ are denoted by $\mathbf{P}_{n,a}$ with the subscript a being the local index in the set. Using the same manner of notation, we can rewrite the initial control points of the patch (Eq. (7)) as

$$\mathbb{P}_0 = \{\mathbf{P}_{0,0}, \mathbf{P}_{0,1}, \ldots, \mathbf{P}_{0,2\kappa+6}, \mathbf{P}_{0,2\kappa+7}\} \tag{9}$$

where the first subscript of $\mathbf{P}$ means the control points corresponding to subdivision level 0.

Each sub-element $\Omega_{n,k}$ also has a set of control points, which is denoted by $\mathbb{Q}_{n,k}$ in which the subscript n stands for the subdivision level and k the sub-element index. We define $\mathbf{Q}_{n,k,a}$ as the points in the set of $\mathbb{Q}_{n,k}$ with the subscript a indicating the local index. To evaluate the target point in a regular sub-element, we need to pick 16 control points for it from $\mathbb{P}_n$,

$$\mathbb{Q}_{n,k} = \boldsymbol{D}_k\mathbb{P}_n, \qquad k = 1, 2, 3 \tag{10}$$

where $\boldsymbol{D}_k$ is a selection operator for regular sub-elements $\Omega_{n,k}(k = 1, 2, 3)$, and $\mathbb{P}_n$ can be generated from the control points of the irregular sub-element at subdivision level $n-1$

$$\mathbb{P}_n = \boldsymbol{A}\mathbb{Q}_{n-1,4} \tag{11}$$

where $\boldsymbol{A}$ is subdivision operator [48,49], and $\mathbb{Q}_{n-1,4}$ collects the control points of $\Omega_{n-1,4}$. $\mathbb{Q}_{n-1,4}$ contains $2\kappa+8$ points and can be calculated from the initial patch control point set $\mathbb{P}_0$ as

$$\mathbb{Q}_{n-1,4} = \bar{\boldsymbol{A}}\mathbb{Q}_{n-2,4} = \bar{\boldsymbol{A}}^{n-1}\mathbb{P}_0 \tag{12}$$

where $\bar{\boldsymbol{A}}$ is a square matrix operator as detailed in [48,49]

Hence, the control point set $\mathbb{Q}_{n,k}$ of the regular sub-element $\Omega_{n,k}$ $(k = 1, 2, 3)$ at subdivision level n is computed from $\mathbb{P}_0$:

$$\mathbb{Q}_{n,k} = \boldsymbol{D}_k\boldsymbol{A}\bar{\boldsymbol{A}}^{n-1}\mathbb{P}_0 \tag{13}$$

where $\boldsymbol{D}_k$ is a selection operator to pick control points for the sub-elements, and $\mathbb{Q}_{n,k}$ contains 16 control points.

After aforementioned subdivision operations, and the target point in the irregular element can be computed as

$$\mathbf{x}(\xi,\eta) = \sum_{a=0}^{15} N_a(\bar{\xi},\bar{\eta})\,\mathbf{Q}_{n,k,a}, \qquad k = 1, 2, 3 \tag{14}$$

where $(\bar{\xi}, \bar{\eta})$ means the parametric coordinates of the evaluated point in the sub-element, which can be mapped from (ξ, η) as

$$(\bar{\xi},\bar{\eta}) = \begin{cases} (2^n\xi - 1, 2^n\eta) & \text{if} \quad k = 1 \\ (2^n\xi - 1, 2^n\eta - 1) & \text{if} \quad k = 2 \\ (2^n\xi, 2^n\eta - 1) & \text{if} \quad k = 3 \end{cases} \tag{15}$$

Considering Eqs. (10)–(13), we rewrite Eq. (14) in the parametric coordinate system of the patch as

$$\mathbf{x}(\xi,\eta) = \sum_{a=0}^{2\kappa+7} \hat{N}_a(\xi,\eta)\,\mathbf{P}_{0,a} \tag{16}$$

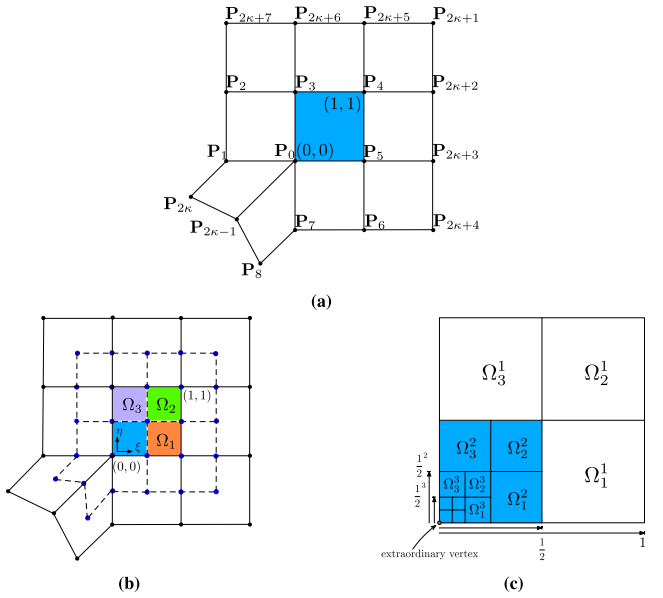

Fig. 4. (a) An irregular patch for an element (blue) with an extraordinary vertex at its lower-left corner. (b) A subdivision of the element patch divides the element into four sub-elements; $\Omega_{1,1}, \Omega_{1,2}$ and $\Omega_{1,3}$ are in regular patches. Blue vertices represent the updated patch control points ($\mathbb{P}_1$). (c) Repeated subdivision of the parametric domain for evaluating point close to an extraordinary vertex. (For interpretation of the references to color in this figure legend, the reader is referred to the web version of this article.)

where $\hat{N}$ is the Catmull–Clark subdivision surfaces basis function. We define $\hat{\mathbf{N}}$ as a set of $2\kappa+8$ basis functions, $\hat{N}_a$, which can be calculated in a vector form as

$$\hat{\mathbf{N}}(\xi,\eta) = [\boldsymbol{D}_k \boldsymbol{A}\bar{\boldsymbol{A}}^{n-1}]^{\mathrm{T}} \mathbf{N}(\bar{\xi},\bar{\eta}) \tag{17}$$

where $\mathbf{N}$ is a set of 16 regular basis functions defined in Eq. (5).

The derivatives of the Catmull–Clark subdivision surfaces basis functions for elements containing extraordinary vertex can be computed by

$$\begin{aligned} \frac{\partial \hat{\mathbf{N}}(\xi,\eta)}{\partial \xi} &= 2^n [\boldsymbol{D}_k \boldsymbol{A}\bar{\boldsymbol{A}}^{n-1}]^{\mathrm{T}} \frac{\partial \mathbf{N}(\bar{\xi},\bar{\eta})}{\partial \bar{\xi}}, \\ \frac{\partial \hat{\mathbf{N}}(\xi,\eta)}{\partial \eta} &= 2^n [\boldsymbol{D}_k \boldsymbol{A}\bar{\boldsymbol{A}}^{n-1}]^{\mathrm{T}} \frac{\partial \mathbf{N}(\bar{\xi},\bar{\eta})}{\partial \bar{\eta}} \end{aligned} \tag{18}$$

In this example, the original irregular element contains only one extraordinary vertex. However, the algorithm is still applicable to the irregular elements with multiple extraordinary vertices. After subdivision, any sub-element contains at most one extraordinary vertex.

3. Structure-acoustic interaction

Consider an acoustic-structure interaction system, as shown in Fig. 5. Ω_s denotes the elastic thin shell structure immersed in an infinite fluid domain Ω_f. $\Gamma_{sf} := \Omega_s \cap \Omega_f$ denotes the coupling surface between structure and fluid. The enclosed shell is filled with air Ω_a. Because the air density is far less than the structural density, the influence of the air pressure on the structural vibration can be ignored. Kirchhoff–Love shell theory governs the behavior of thin shell structures. The radiation acoustic pressure in the fluid domain is governed by the Helmholtz equation. The structure is excited by a time-harmonic force with an angular frequency ω. So acoustic-structure interaction analysis is essentially finding the solution of the following coupled equations:

$$\nabla \cdot \boldsymbol{\sigma}(\mathbf{x}) + \omega^2 \rho_s \mathbf{u}(\mathbf{x}) = 0 \qquad \mathbf{x} \in \Omega_s \tag{19}$$

$$\nabla^2 p(\mathbf{x}) + k^2 p(\mathbf{x}) = 0 \qquad \mathbf{x} \in \Omega_f \tag{20}$$

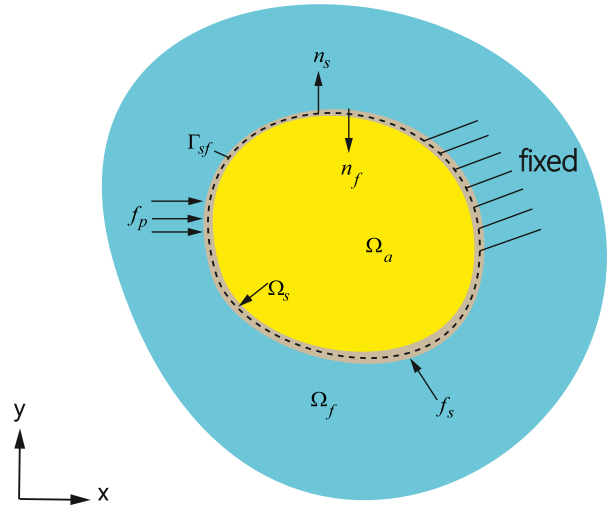

Fig. 5. Acoustic-structure interaction system. n_s and n_f are the unit normal vectors of shell structure and fluid, respectively. The mid-surface of the shell structure is presented by a dashed line. f_s is external mechanical load and f_p is sound field pressure load.

$$\boldsymbol{\sigma}(\mathbf{x}) \cdot \mathbf{n}_s(\mathbf{x}) - p(\mathbf{x}) \mathbf{n}_f(\mathbf{x}) = 0 \qquad \mathbf{x} \in \Gamma_{sf} \tag{21}$$

$$-\mathrm{i}\omega \mathbf{u}(\mathbf{x}) \cdot \mathbf{n}_f(\mathbf{x}) = v_f^n(\mathbf{x}) \qquad \mathbf{x} \in \Gamma_{sf} \tag{22}$$

Eqs. (19) and (20) are the governing equations of structure and sound fields, respectively. Eqs. (21) and (22) represent the conditions of force balance and displacement continuity on the coupling surface, respectively. In the above equations, the symbol ∇ stands for the Laplace operator, $\boldsymbol{\sigma}$ the stress tensor, $\mathbf{u}$ the displacements, ρ_s the density of the shell, $p(\mathbf{x})$ the sound pressure, $\mathbf{n}_s$ and $\mathbf{n}_f$ the outward and inward normal vectors of the shell surfaces, respectively, v_f^n the normal velocity of the fluid, $\mathrm{i} = \sqrt{-1}$ the imaginary unit, and k the wave number that is equal to $\frac{\omega}{c}$ in which c is the propagation velocity of an acoustic wave in the fluid domain.

In the following subsections, we will formulate the isogeometric shell finite element method (IGAFEM) with subdivision surface for structure analysis, and the isogeometric boundary element method (IGABEM) with subdivision surface for acoustic analysis.

3.1. IGAFEM for thin-shells with Catmull–Clark subdivision surfaces

The variational formulation of a Kirchhoff–Love shell based on the principle of virtual work reads

$$\delta W = \delta W_{\mathrm{mas}} + \delta W_{\mathrm{int}} + \delta W_{\mathrm{ext}} = 0 \tag{23}$$

The three terms δW_{mas}, δW_{int} and δW_{ext} denote the virtual work contributions of the inertia, internal and external forces, respectively. Because the mid-surface displacements $\mathbf{u}$ is assumed to be time harmonic, the virtual inertia work δW_{mas} can be expressed by

$$\delta W_{\mathrm{mas}} = \int_\Gamma \rho_s \frac{\partial^2 \mathbf{u}}{\partial t^2} \cdot \delta \mathbf{u} h \mathrm{d}\Gamma = -\omega^2 \int_\Gamma \rho_s \mathbf{u} \cdot \delta \mathbf{u} h \mathrm{d}\Gamma \tag{24}$$

where $\delta \mathbf{u}$ denotes the virtual displacements, h the shell thickness and $\Gamma = \Gamma_{sf}$.

A fundamental assumption of the Kirchhoff–Love theory is that the straight lines normal to the mid-surface of a shell remain straight and normal to the mid-surface after deformation, which implies that the in-plane strain is linearly distributed through the thickness and the transverse shear strains are zero. By separating the stresses into a membrane and a bending part and integrating through the thickness, the internal virtual work can be written as

$$\delta W_{\mathrm{int}} = \int_\Gamma \left(\frac{1}{2} \frac{Eh}{1-\upsilon^2} \delta \boldsymbol{\varepsilon}^{\mathrm{T}} \mathbf{D} \boldsymbol{\varepsilon} + \frac{1}{2} \frac{Eh^3}{12\left(1-\upsilon^2\right)} \delta \boldsymbol{\kappa}^{\mathrm{T}} \mathbf{D} \boldsymbol{\kappa} \right) \mathrm{d}\Gamma \tag{25}$$

in which

$$\mathbf{D}=\begin{pmatrix} \left(\bar{a}^{11}\right)^2 & v\bar{a}^{11}\bar{a}^{-22}+(1-v)\left(\bar{a}^{12}\right)^2 & \bar{a}^{11}\bar{a}^{12} \\ & \left(\bar{a}^{22}\right)^2 & \bar{a}^{22}\bar{a}^{12} \\ \text{sym.} & & \frac{1}{2}\left[(1-v)\bar{a}^{11}\bar{a}^{22}+(1+v)\left(\bar{a}^{12}\right)^2\right] \end{pmatrix} \tag{26}$$

where E is Young's modulus and v is Poisson's ratio, and $\bar{a}^{11}$, $\bar{a}^{22}$, $\bar{a}^{12}$ are the components of the covariant tensor of the middle surface. $\boldsymbol{\varepsilon}$ and $\boldsymbol{\kappa}$ are the membrane and bending strains, respectively, whose components are defined as

$$\varepsilon_{ij}=\frac{1}{2}\left(\bar{\mathbf{a}}_i\cdot\mathbf{u}_{,j}+\mathbf{u}_{,i}\cdot\bar{\mathbf{a}}_j\right) \tag{27}$$

and

$$\begin{aligned}\kappa_{ij}=&-\mathbf{u}_{,ij}\cdot\bar{\mathbf{a}}_3+\frac{1}{\sqrt{\bar{a}}}\left(\mathbf{u}_{,1}\cdot\left(\bar{\mathbf{a}}_{i,j}\times\bar{\mathbf{a}}_2\right)+\mathbf{u}_{,2}\cdot\left(\bar{\mathbf{a}}_1\times\bar{\mathbf{a}}_{i,j}\right)\right)\\&+\frac{\bar{\mathbf{a}}_3\cdot\bar{\mathbf{a}}_{i,j}}{\sqrt{\bar{a}}}\left(\mathbf{u}_{,1}\cdot\left(\bar{\mathbf{a}}_2\times\bar{\mathbf{a}}_3\right)+\mathbf{u}_{,2}\cdot\left(\bar{\mathbf{a}}_3\times\bar{\mathbf{a}}_1\right)\right)\end{aligned} \tag{28}$$

where a comma is used to denote partial differentiation, $\bar{\mathbf{a}}_i$ is the surface basis vector in the reference configuration, and $\sqrt{\bar{a}}=|\bar{\boldsymbol{a}}_1\times\bar{\boldsymbol{a}}_2|$.

The external virtual work is given by

$$\delta W_{\text{ext}}=-\int_{\Gamma}p\mathbf{n}_s\cdot\delta\mathbf{u}\mathrm{d}\Gamma \tag{29}$$

where $\mathbf{n}_s$ stands for the normal vector at the mid-surface point, and p is the pressure enforced on the mid-surface.

The subdivision surface is used to construct the structural model and discretize structural domain. The boundary Γ is defined through the union of elements, as follows

$$\Gamma=\bigcup_{e=1}^{n_{fe}}\Gamma_e \tag{30}$$

where the set of elements $\{\Gamma_e\}_{e=1}^{n_{fe}}$ is the tessellation of the Catmull–Clark subdivision surface scheme, n_{fe} is the number of elements and Γ_e is the eth element. Thus, the displacement is discretized with Catmull–Clark subdivision basis functions N_s^e, as follows

$$\tilde{\mathbf{u}}^e=\sum_{a=0}^{2\kappa+7}\hat{N}_a(\xi,\eta)\tilde{\mathbf{u}}_a^e \tag{31}$$

where $\tilde{\mathbf{u}}_a^e$ denotes the nodal parameters associated with the ath control point at the patch of the eth element for discretizing the displacements.

By assembling all the element matrices, we can obtain the following equation

$$\mathbf{A}\tilde{\mathbf{u}}=\mathbf{f} \tag{32}$$

with

$$\mathbf{A}=\mathbf{K}-\omega^2\mathbf{M},\quad \mathbf{K}=\bigcup_{e=1}^{N_{fe}}\mathbf{K}^e,\quad \mathbf{M}=\bigcup_{e=1}^{N_{fe}}\mathbf{M}^e \tag{33}$$

where $\mathbf{K}$, $\mathbf{M}$ are the global stiffness matrix and mass matrix of the structure, $\mathbf{K}^e$ and $\mathbf{M}^e$ are the element stiffness matrix and mass matrix, $\tilde{\mathbf{u}}$ is the displacement vector of all the vertices, and $\mathbf{f}$ is the load vector that is composed of external mechanical load $\mathbf{f}_s$ and sound field pressure load $\mathbf{f}_p$ as follows

$$\mathbf{f}=\mathbf{f}_s+\mathbf{f}_p \tag{34}$$

3.2. Boundary element formulations with Catmull–Clark subdivision surfaces

The Helmholtz equation governing the time harmonic acoustic wave propagation in domain $\Omega\in\mathbb{R}^3$ with boundary Γ can be transformed to the following boundary integral equation

$$C(\mathbf{x})p(\mathbf{x})+\int_{\Gamma}\frac{\partial G(\mathbf{x},\mathbf{y})}{\partial n_f(\mathbf{y})}p(\mathbf{y})\mathrm{d}\Gamma=\int_{\Gamma}G(\mathbf{x},\mathbf{y})q(\mathbf{y})\mathrm{d}\Gamma \tag{35}$$

where $C(\mathbf{x})$ is the jump term that equals $\frac{1}{2}$ for smooth surfaces, $q(\mathbf{y})=\frac{\partial p(\mathbf{y})}{\partial n_f(\mathbf{y})}$ represents sound pressure flux, $n_f(\mathbf{y})$ is a unit outward normal to Γ. $G(\mathbf{x},\mathbf{y})=\frac{\mathrm{e}^{\mathrm{i}kr}}{4\pi r}$ denotes the Green's function for the 3D Helmholtz equation, where $r=|\mathbf{x}-\mathbf{y}|$ and $\mathrm{i}=\sqrt{-1}$.

Using Eq. (35) alone for simulating exterior acoustic field may lead to non-uniqueness of the solution at the fictitious eigenfrequencies. This problem can be solved with Burton–Miller formulation [20,50], which is formulated by linear combination of Eq. (35) and its normal derivative. By differentiating Eq. (35) with respect to the normal $n_f(\mathbf{x})$, we arrive at

$$C(\mathbf{x})q(\mathbf{x})+\int_{\Gamma}\frac{\partial^2 G(\mathbf{x},\mathbf{y})}{\partial n_f(\mathbf{x})\partial n_f(\mathbf{y})}p(\mathbf{y})\mathrm{d}\Gamma=\int_{\Gamma}\frac{\partial G(\mathbf{x},\mathbf{y})}{\partial n_f(\mathbf{x})}q(\mathbf{y})\mathrm{d}\Gamma \tag{36}$$

The linear combination of Eqs. (35) and (36) is expressed by

$$\begin{aligned}&C(\mathbf{x})p(\mathbf{x})+\alpha C(\mathbf{x})q(\mathbf{x})+\int_{\Gamma}\frac{\partial G(\mathbf{x},\mathbf{y})}{\partial n_f(\mathbf{y})}p(\mathbf{y})\mathrm{d}\Gamma+\alpha\int_{\Gamma}\frac{\partial^2 G(\mathbf{x},\mathbf{y})}{\partial n_f(\mathbf{x})\partial n_f(\mathbf{y})}p(\mathbf{y})\mathrm{d}\Gamma\\&=\int_{\Gamma}G(\mathbf{x},\mathbf{y})q(\mathbf{y})\mathrm{d}\Gamma+\alpha\int_{\Gamma}\frac{\partial G(\mathbf{x},\mathbf{y})}{\partial n_f(\mathbf{x})}q(\mathbf{y})\mathrm{d}\Gamma\end{aligned} \tag{37}$$

where α is the combining parameter: $\alpha=\mathrm{i}/k$ for $k>1$, and $\alpha=\mathrm{i}$ otherwise.

In this work, the subdivision surface basis functions used for geometry construction are employed for discretizing the physical field:

$$\begin{aligned}p_e&=\sum_{a=0}^{2\kappa+7}\hat{N}_a(\xi,\eta)\tilde{p}_a^e\\q_e&=\sum_{a=0}^{2\kappa+7}\hat{N}_a(\xi,\eta)\tilde{q}_a^e\end{aligned} \tag{38}$$

where p_e and q_e represent the sound pressure and its normal flux at a point (ξ,η) located in the element Γ_e, and $\tilde{p}_a^e$ and $\tilde{q}_a^e$ are the nodal parameters associated with the sound pressure and its normal flux corresponding to a control point in the patch of the Γ_e element, respectively. By substituting Eq. (38) into Eq. (37) and enforcing the equations at a discrete set of collocation points $(\mathbf{x}_c)$, we have the following linear system of equations

$$\begin{aligned}&C(\mathbf{x}_c)p(\mathbf{x}_c)+\alpha C(\mathbf{x}_c)q(\mathbf{x}_c)+\sum_{e=1}^{N_e}\sum_{a=0}^{2\kappa+7}\int_{\Gamma_e}\hat{N}_a(\xi,\eta)\frac{\partial G(\mathbf{x}_c,\mathbf{y}(\xi,\eta))}{\partial n_f(\mathbf{y}(\xi,\eta))}\mathrm{d}\Gamma\tilde{p}_a^e\\&\quad+\alpha\sum_{e=1}^{N_e}\sum_{a=0}^{2\kappa+7}\int_{\Gamma_e}\hat{N}_a(\xi,\eta)\frac{\partial^2 G(\mathbf{x}_c,\mathbf{y}(\xi,\eta))}{\partial n_f(\mathbf{x}_c)\partial n_f(\mathbf{y}(\xi,\eta))}\mathrm{d}\Gamma\tilde{p}_a^e\\&=\sum_{e=1}^{N_e}\sum_{a=0}^{2\kappa+7}\int_{\Gamma_e}\hat{N}_a(\xi,\eta)G(\mathbf{x}_c,\mathbf{y}(\xi,\eta))\mathrm{d}\Gamma\tilde{q}_a^e\\&\quad+\alpha\sum_{e=1}^{N_e}\sum_{a=0}^{2\kappa+7}\int_{\Gamma_e}\hat{N}_a(\xi,\eta)\frac{\partial G(\mathbf{x}_c,\mathbf{y}(\xi,\eta))}{\partial n_f(\mathbf{x}_c)}\mathrm{d}\Gamma\tilde{q}_a^e\end{aligned} \tag{39}$$

where the subscript c indicates the collocation point number. Because the control points may not lie in the surface, the collocation points are generated by mapping the control points to the surface. Eq. (39) can be recast in matrix–vector form as

$$\mathbf{H}\tilde{\mathbf{p}}=\mathbf{G}\tilde{\mathbf{q}} \tag{40}$$

where $\mathbf{H}$ and $\mathbf{G}$ are the coefficient matrices, and $\tilde{\mathbf{p}}$ and $\tilde{\mathbf{q}}$ are the column vectors that collect nodal parameters associated with sound pressure and its flux, respectively. It is worth noting that the singular integrals exist in Eq. (37), and special attention needs to be paid. Several methods have been proposed to deal with the singular integrals in BEM [51–55]. In this work, Guiggiani method is used for numerical evaluation of general boundary element integrals, please see [51,56] for detailed information.

3.3. Coupled formulations with Catmull–Clark subdivision surfaces

Eq. (32) obtained by the structural finite element method and Eq. (40) by the acoustic boundary element method cannot be solved

separately. They are coupled together through the boundary conditions defined in Eqs. (21) and (22). The acoustic pressure in the fluid domain can be treated as a force imposed on the shell, which is directed along the inward normal of the surface. Hence, the nodal force vector of acoustic load $\mathbf{f}_p$ in Eq. (34) can be written as

$$\mathbf{f}_p = \tilde{\mathbf{n}}_f \Theta \tilde{\mathbf{p}} \tag{41}$$

where $\Theta = \int_\Gamma \hat{\mathbf{N}}^{\mathrm{T}} \hat{\mathbf{N}} \mathrm{d}\Gamma$, $\hat{\mathbf{N}}$ is the global vector of subdivision basis functions, and $\tilde{\mathbf{n}}_f$ is the matrix of normals that are defined as:

$$\tilde{\mathbf{n}}_f = \begin{Bmatrix} n_{1f}\cdot e_1 & 0 & \dots \\ n_{1f}\cdot e_2 & 0 & \dots \\ n_{1f}\cdot e_3 & 0 & \dots \\ 0 & n_{2f}\cdot e_1 & \dots \\ 0 & n_{2f}\cdot e_2 & \dots \\ 0 & n_{2f}\cdot e_3 & \dots \\ \dots & \dots & \dots \end{Bmatrix} \tag{42}$$

where e_1, e_2, e_3 are the three orthogonal normal Cartesian base vectors. By substituting Eq. (41) to Eq. (34), the global nodal force vector can be expressed by

$$\mathbf{f} = \mathbf{C}_{sf}\tilde{\mathbf{p}} + \mathbf{f}_s \tag{43}$$

in which $\mathbf{C}_{sf} = \tilde{\mathbf{n}}_f \Theta$.

Now, we consider the relationship between acoustic pressure and shell mid-surface velocities. We denote $\mathbf{v}_f^n$ and $\mathbf{v}_s^n$ as the vectors that collect the nodal parameters associated with the normal components of the fluid and structural velocities, respectively. If there is no energy loss between the structural domain and fluid domain, we have

$$\mathbf{v}_f^n - \mathbf{v}_s^n = 0 \tag{44}$$

in which $\mathbf{v}_s^n = \mathrm{i}\omega \mathbf{C}_{fs}\tilde{\mathbf{u}}$ with $\mathbf{C}_{fs} = \tilde{\mathbf{n}}_f^{\mathrm{T}}$. Then the vector $\tilde{\mathbf{q}}$ that collects the nodal parameters associated with acoustic flux is given by

$$\tilde{\mathbf{q}} = \frac{\partial \tilde{\mathbf{p}}}{\partial n} = -\mathrm{i}\omega\rho_f \mathbf{v}_f^n = \omega^2 \rho_f \mathbf{C}_{fs}\tilde{\mathbf{u}} \tag{45}$$

where ρ_f is the density of fluid.

Upon substitution of Eq. (45) into the boundary element system of equations (Eq. (40)), a coupled system for the acoustic problem is given by

$$\mathbf{H}\tilde{\mathbf{p}} = \mathbf{G}\omega^2\rho_f \mathbf{C}_{fs}\tilde{\mathbf{u}} \tag{46}$$

By substituting Eq. (43) into Eq. (32), a coupled system of equations for the structural dynamics problem is expressed by:

$$\mathbf{A}\tilde{\mathbf{u}} = \mathbf{C}_{sf}\tilde{\mathbf{p}} + \mathbf{f}_s \tag{47}$$

Substituting Eq. (47) into Eq. (46) eliminates the unknown displacement $\tilde{\mathbf{u}}$ and leads to the following boundary element formulation coupled by finite element equation

$$[\mathbf{H} - \mathbf{G}\mathbf{Y}]\,\tilde{\mathbf{p}} = \mathbf{G}\tilde{\mathbf{q}}_s \tag{48}$$

where $\mathbf{Y}$ is a global admittance matrix and $\tilde{\mathbf{q}}_s$ accounts for the contribution of acoustic velocities from the structural domain. They are expressed by

$$\begin{aligned} \mathbf{Y} &= \omega^2\rho_f \mathbf{C}_{fs}\mathbf{A}^{-1}\mathbf{C}_{sf} \\ \tilde{\mathbf{q}}_s &= \omega^2\rho_f \mathbf{C}_{fs}\mathbf{A}^{-1}\mathbf{f}_s \end{aligned} \tag{49}$$

It is worth noting that singular value decomposition (SVD) or modal analysis approach can be used to approximate inverse of matrix $\mathbf{A}$ in Eq. (49). Actually, directly solving the term $\mathbf{A}^{-1}$ is not needed in this work. One can calculate $\mathbf{A}^{-1}\mathbf{f}_s$ in Eq. (49) by solving the algebraic equation $\mathbf{A}\mathbf{x} = \mathbf{f}_s$ using an iterative solver, for example, generalized minimal residual method (GMRES).

4. Topology optimization for acoustic-structure interaction system

A mathematical model of topology optimization for acoustic-structure interaction systems can be expressed by

$$\begin{aligned} \min_{\boldsymbol{\mu}} \quad & \Pi = \Pi(\tilde{\mathbf{u}}, \tilde{\mathbf{p}}) \\ \text{s.t.} \quad & V(\boldsymbol{\mu}) - V_0 \leqslant 0 \\ & \mathbf{A}\tilde{\mathbf{u}} = \mathbf{C}_{sf}\tilde{\mathbf{p}} + \mathbf{f}_s \\ & \mathbf{H}\tilde{\mathbf{p}} = \mathbf{G}\omega^2\rho_f \mathbf{C}_{fs}\tilde{\mathbf{u}} \\ & 0 \leqslant \mu_e \leqslant 1, \quad e = 1, \dots, N_e \end{aligned} \tag{50}$$

where Π is the objective function in terms of $\tilde{\mathbf{u}}$ and $\tilde{\mathbf{p}}$, $\boldsymbol{\mu} = [\mu_1, \mu_2, \dots, \mu_{N_e}]$ represents the number of elements, $V(\boldsymbol{\mu})$ denotes the volume of sound-absorbing materials, and V_0 the prescribed maximum volume.

The most commonly used objective functions in acoustic optimization are the sound pressure in the reference area and the sound power radiated from the structure. Among them, the sound pressure can only reflect the local noise level, whereas the radiated sound power is able to represent the radiated energy level of the whole structure vibration. Therefore, the radiated sound power level (SWL) is often used as the vibration and noise index of the full system in the practical project:

$$\Pi = \Pi(\tilde{\mathbf{u}}, \tilde{\mathbf{p}}) = 10\log\frac{W(\tilde{\mathbf{u}}, \tilde{\mathbf{p}})}{W_0} \tag{51}$$

where W_0 is the reference sound power, and W denotes the radiated sound power that is independent on space and distance from the vibrating structure, as follows

$$W(\tilde{\mathbf{u}}, \tilde{\mathbf{p}}) = -\frac{1}{2}\Re\left(\tilde{\mathbf{p}}^{\mathrm{H}}\Theta\mathbf{v}_f^*\right) = -\frac{1}{2}\Re\left(\tilde{\mathbf{p}}^{\mathrm{H}}\Theta\mathbf{v}_f\right) = -\frac{1}{2}\Re\left(\mathrm{i}\omega\tilde{\mathbf{p}}^{\mathrm{H}}\Theta\mathbf{C}_{fs}\tilde{\mathbf{u}}\right) \tag{52}$$

where $\Re$ indicates the real part, $()^*$ stands for conjugate complex, and $()^{\mathrm{H}}$ represents conjugation after transposition.

Sensitivity analysis of the objective function directly determines the reliability and efficiency of the optimization. To handle a large number of design variables, the adjoint variable method is employed in the present work. We first rewrite the objective function by adding the zero function:

$$\tilde{\Pi} = \Pi + \Re\left[\lambda_1^{\mathrm{T}}\left(\mathbf{A}\tilde{\mathbf{u}} - \mathbf{f}_s - \mathbf{C}_{sf}\tilde{\mathbf{p}}\right) + \lambda_2^{\mathrm{T}}\left(\mathbf{H}\tilde{\mathbf{p}} - \mathbf{G}\omega^2\rho_f\mathbf{C}_{fs}\tilde{\mathbf{u}}\right)\right] \tag{53}$$

where λ_1 and λ_2 are adjoint variable vectors, whose values can be arbitrarily selected to maintain $\tilde{\Pi} = \Pi$ because $\mathbf{A}\tilde{\mathbf{u}} - \mathbf{f}_s - \mathbf{C}_{sf}\tilde{\mathbf{p}} = 0$ and $\mathbf{H}\tilde{\mathbf{p}} - \mathbf{G}\omega^2\rho_f\mathbf{C}_{fs}\tilde{\mathbf{u}} = 0$.

Then the derivative of the objective function in Eq. (53) with respect to any design variable μ_e is written as

$$\begin{aligned} \frac{\partial\tilde{\Pi}}{\partial\mu_e} =& \Re\left\{\mathbf{z}_1^{\mathrm{T}}\frac{\partial\tilde{\mathbf{u}}}{\partial\mu_e} + \mathbf{z}_2^{\mathrm{T}}\frac{\partial\tilde{\mathbf{p}}}{\partial\mu_e} + z_3\right\} + \\ & \Re\left\{\frac{\partial\lambda_1^{\mathrm{T}}}{\partial\mu_e}\left(\mathbf{A}\tilde{\mathbf{u}} - \mathbf{f}_s - \mathbf{C}_{sf}\tilde{\mathbf{p}}\right) + \lambda_1^{\mathrm{T}}\left[\frac{\partial\mathbf{A}}{\partial\mu_e}\tilde{\mathbf{u}} + \mathbf{A}\frac{\partial\tilde{\mathbf{u}}}{\partial\mu_e} - \frac{\partial\mathbf{f}_s}{\partial\mu_e} - \frac{\partial\mathbf{C}_{sf}}{\partial\mu_e}\tilde{\mathbf{p}} - \mathbf{C}_{sf}\frac{\partial\tilde{\mathbf{p}}}{\partial\mu_e}\right]\right\} + \\ & \Re\left\{\frac{\partial\lambda_2^{\mathrm{T}}}{\partial\mu_e}\left(\mathbf{H}\tilde{\mathbf{p}} - \mathbf{G}\omega^2\rho_f\mathbf{C}_{fs}\tilde{\mathbf{u}}\right)\right. \\ & \left. + \lambda_2^{\mathrm{T}}\left[\frac{\partial\mathbf{H}}{\partial\mu_e}\tilde{\mathbf{p}} + \mathbf{H}\frac{\partial\tilde{\mathbf{p}}}{\partial\mu_e} - \omega^2\rho_f\frac{\partial\mathbf{G}\mathbf{C}_{fs}}{\partial\mu_e}\tilde{\mathbf{u}} - \mathbf{G}\omega^2\rho_f\mathbf{C}_{fs}\frac{\partial\tilde{\mathbf{u}}}{\partial\mu_e}\right]\right\} \end{aligned} \tag{54}$$

where $\mathbf{z}_1^{\mathrm{T}} = -\frac{\mathrm{i}\omega 5}{W\ln 10}\tilde{\mathbf{p}}^{\mathrm{H}}\Theta\mathbf{C}_{fs}$, $\mathbf{z}_2^{\mathrm{T}} = \frac{\mathrm{i}\omega 5}{W\ln 10}\tilde{\mathbf{u}}^{\mathrm{H}}\mathbf{C}_{sf}$, and $z_3 = 0$, and the terms $\frac{\partial\mathbf{f}_s}{\partial\mu_e}$, $\frac{\partial\mathbf{C}_{sf}}{\partial\mu_e}$, $\frac{\partial\mathbf{H}}{\partial\mu_e}$, $\frac{\partial\mathbf{G}}{\partial\mu_e}$, and $\frac{\partial\mathbf{C}_{fs}}{\partial\mu_e}$ vanish because they are independent of design variables. Thus, Eq. (54) can in turn be written as

$$\begin{aligned} \frac{\partial\tilde{\Pi}}{\partial\mu_e} =& \Re\left\{\mathbf{z}_1^{\mathrm{T}}\frac{\partial\tilde{\mathbf{u}}}{\partial\mu_e} + \mathbf{z}_2^{\mathrm{T}}\frac{\partial\tilde{\mathbf{p}}}{\partial\mu_e} + \lambda_1^{\mathrm{T}}\left(\frac{\partial\mathbf{A}}{\partial\mu_e}\tilde{\mathbf{u}} + \mathbf{A}\frac{\partial\tilde{\mathbf{u}}}{\partial\mu_e} - \mathbf{C}_{sf}\frac{\partial\tilde{\mathbf{p}}}{\partial\mu_e}\right)\right\} + \\ & \Re\left\{\lambda_2^{\mathrm{T}}\left[\mathbf{H}\frac{\partial\tilde{\mathbf{p}}}{\partial\mu_e} - \omega^2\rho_f\mathbf{G}\mathbf{C}_{fs}\frac{\partial\tilde{\mathbf{u}}}{\partial\mu_e}\right]\right\} \end{aligned} \tag{55}$$

After rearrangement of the terms, Eq. (55) can be rewritten as

$$\frac{\partial\tilde{\Pi}}{\partial\mu_e} = \Re\left\{\left[\mathbf{z}_1^{\mathrm{T}} + \lambda_1^{\mathrm{T}}\mathbf{A} - \lambda_2^{\mathrm{T}}\omega^2\rho_f\mathbf{G}\mathbf{C}_{fs}\right]\frac{\partial\tilde{\mathbf{u}}}{\partial\mu_e}\right\} +$$

$$\Re\left\{\left[\mathbf{z}_2^{\mathrm{T}}-\lambda_1^{\mathrm{T}}\mathbf{C}_{sf}+\lambda_2^{\mathrm{T}}\mathbf{H}\right]\frac{\partial\tilde{\mathbf{p}}}{\partial\mu_e}+\lambda_1^{\mathrm{T}}\frac{\partial\mathbf{A}}{\partial\mu_e}\tilde{\mathbf{u}}\right\} \tag{56}$$

By letting the adjoint variables satisfy the following adjoint equations

$$\begin{aligned}&\mathbf{z}_2^{\mathrm{T}}-\lambda_1^{\mathrm{T}}\mathbf{C}_{sf}+\lambda_2^{\mathrm{T}}\mathbf{H}=0\\&\mathbf{z}_1^{\mathrm{T}}+\lambda_1^{\mathrm{T}}\mathbf{A}-\omega^2\rho_f\lambda_2^{\mathrm{T}}\mathbf{G}\mathbf{C}_{fs}=0\end{aligned} \tag{57}$$

the derivative of objective function with respect to any design variable can be expressed as a function of the adjoint variables as follows

$$\frac{\partial\Pi}{\partial\mu_e}=\frac{\partial\tilde{\Pi}}{\partial\mu_e}=\Re\left(\lambda_1^{\mathrm{T}}\frac{\partial\mathbf{A}}{\partial\mu_e}\tilde{\mathbf{u}}\right) \tag{58}$$

Hence, a key step in sensitivity analysis with adjoint variable methods is to evaluate the adjoint variable by solving the adjoint equation (Eq. (57)). Upon substitution of the second formulation of Eq. (57) into its first formulation, we obtain that

$$\lambda_2^{\mathrm{T}}\left(\mathbf{G}\mathbf{Y}-\mathbf{H}\right)=\mathbf{z}_2^{\mathrm{T}}+\mathbf{z}_1^{\mathrm{T}}\mathbf{A}^{-1}\mathbf{C}_{sf} \tag{59}$$

By using GMRES to solve Eq. (59), we can obtain solution of λ_2^{T}. Using the second formulation in Eq. (57) again, λ_1^{T} can be computed as

$$\lambda_1^{\mathrm{T}}=\left(\omega^2\rho_f\lambda_2^{\mathrm{T}}\mathbf{G}\mathbf{C}_{fs}-\mathbf{z}_1^{\mathrm{T}}\right)\mathbf{A}^{-1} \tag{60}$$

It is worth noting that the adjoint variable λ_1 is independent of the design variables, so the adjoint equation needs to be solved only once to get the sensitivities for all of the design variables.

After the sensitivity analysis, the gradients are used in the method of moving asymptote (MMA) [57] to realize the continuous updating of design variables. The iteration converges when the relative error between the objective functions of two adjacent iterations is less than a certain value:

$$\text{change}=\frac{\left|\Pi^{j+1}-\Pi^{j}\right|}{\Pi^{j}}<\tau \tag{61}$$

where Π^j represents the objective function value of the jth step in the optimization process, and τ denotes the convergence tolerance.

In this work, the design variables μ_e are the parameters corresponding to the state of the structural elements. The density-based topology optimization algorithm is used herein. The material parameters of every structural element can be represented by the exponential function of artificial density. For example, the elastic modulus and density of the material are expressed as

$$\begin{aligned}&E(\mu_e)=E_1+\mu_e^{\eta_1}(E_2-E_1),\\&\rho(\mu_e)=\rho_1+\mu_e^{\eta_2}(\rho_2-\rho_1)\end{aligned} \tag{62}$$

where $\mu_e\in[0,1]$, η_1 and η_2 are penalization factors, (E_1,ρ_1) and (E_2,ρ_2) denote elastic modulus and density of two different materials, respectively.

5. Numerical examples

In this section, several numerical tests are presented to investigate the correctness and validity of this proposed algorithm. The code for solving acoustic-structure interaction system is written using Fortran 90 language and run on a PC with an Intel(R) Core(TM) i7-7700 CPU and 8 GB RAM. To investigate the validity and applicability of the proposed algorithm for topology optimization, several numerical examples are presented in this section. The tolerances of GMRES is set to be 10^{-4}, and the iterative convergence criterion τ is set to be 10^{-5}. The objective functions in all optimization examples are set as radiated sound power level (SWL) presented in Eq. (51).

5.1. Elastic spherical shell excited by a unit force

In this subsection, the correctness and effectiveness of the proposed algorithm are verified by using an example with analytical solution. This subsection is devoted to verify the numerical analysis of coupling effects. The topology optimization will be studied in the following subsections. The vibration response analysis of a submerged elastic spherical shell excited by a harmonic point excitation $F=F_0e^{-\mathrm{i}\omega t}$ is taken as a test example, as shown in Fig. 6. Speed of sound in the water is 1482 m/s. Point A is the load action point. The viscous resistance of water to the structure balances the concentrated load and keeps the whole position of the structure unchanged. The distribution of viscous resistance on a sphere is given in [27], as follows

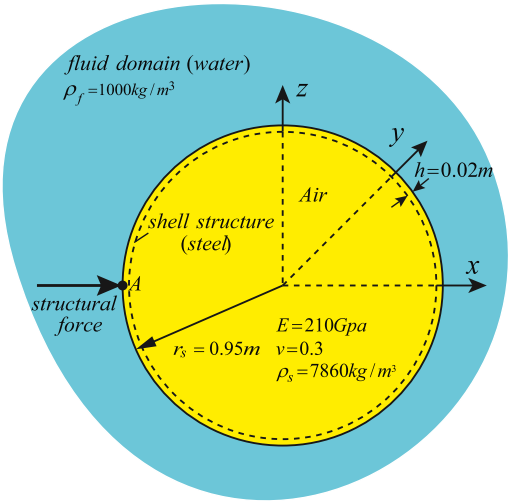

Fig. 6. Acoustic-structure interaction system of a sphere shell excited by a force in an infinite fluid domain. The sphere shell with a radius r_s= 0.95 m is filled with air. Parameter for geometry and material properties can be seen.

$$f_a=\sum_n f_n p_n(\cos\theta)e^{-\mathrm{i}\omega t} \tag{63}$$

where

$$f_n=\frac{(2n+1)F_0}{4\pi r_s^2} \tag{64}$$

The solution to this test can be obtained analytically which we reproduce for completeness herein. The angle θ represents the central angle between the field point and the point of excitation. The sound pressure $p(\theta)$ and the displacement $u(\theta)$ at the spherical surface, respectively, are given as

$$p(\theta)=\frac{F}{4\pi r_s^2}\sum_{n=0}^{\infty}\frac{(2n+1)z_n}{Z_n+z_n}P_n(cos\theta) \tag{65}$$

and

$$u(\theta)=-\frac{F}{4\pi r_s^2\mathrm{i}\omega}\sum_{n=0}^{\infty}\frac{2n+1}{Z_n+z_n}P_n(cos\theta) \tag{66}$$

where P_n is the nth Legendre function. The modal specific acoustic radiation impedance z_n and the invacuo modal impedance of shell Z_n can be obtained in [27].

The sound pressure $p(R,\theta)$ at a point (R,θ) in fluid domain is given as

$$p(R,\theta)=\frac{\mathrm{i}\rho cF_0}{4\pi r_s^2}\sum_{n=0}^{\infty}\frac{(2n+1)}{(Z_n+z_n)}h_n(kR)P_n(cos\theta)\left(\frac{\partial h_n(kr_s)}{\partial(kr_s)}\right)^{-1} \tag{67}$$

where h_n is the nth Hankel function.

Using Eq. (51) and considering the axisymmetry along the x axis, the radiated sound power is derived by

$$\begin{aligned}P&=\pi r_s^2\int_0^{\pi}\Re\left\{p(\theta)v_f^*(\theta)\right\}\sin(\theta)d\theta\\&\approx\frac{\pi^2r_s^2}{n}\sum_{m=1}^{n}\Re\left\{p(\theta_m)v_f^*(\theta_m)\right\}\sin(\theta_m)\end{aligned} \tag{68}$$

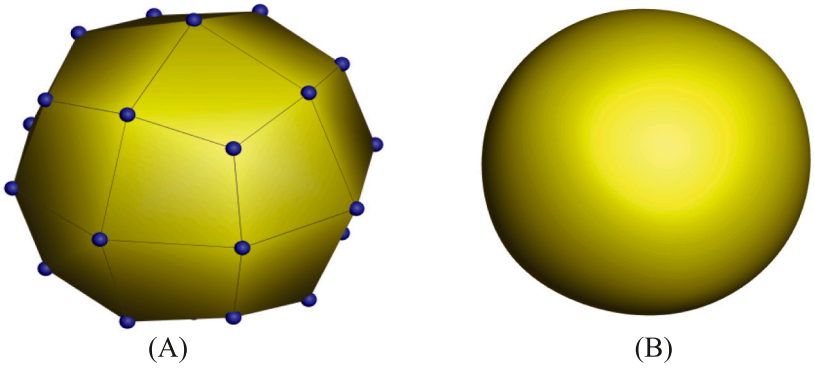

Fig. 7. Meshes of sphere model. (A) the initial coarse Catmull–Clark subdivision discretization with 98 vertices used to generate control meshes, where the initial control vertices are located on a sphere with a radius $r = 1$ m; (B) the limited surface with 6146 vertices.

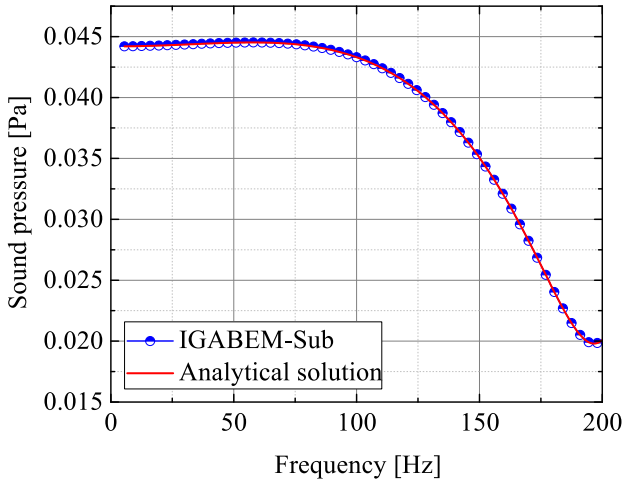

Fig. 8. Comparison between the analytical results and numerical results obtained by the IGA-FEM/BEM with subdivision surface and with the Burton–Miller boundary integral equations (BM) for the sound pressure, calculated at (2r,0,0) as function of frequency. The frequency step is 0.1 Hz.

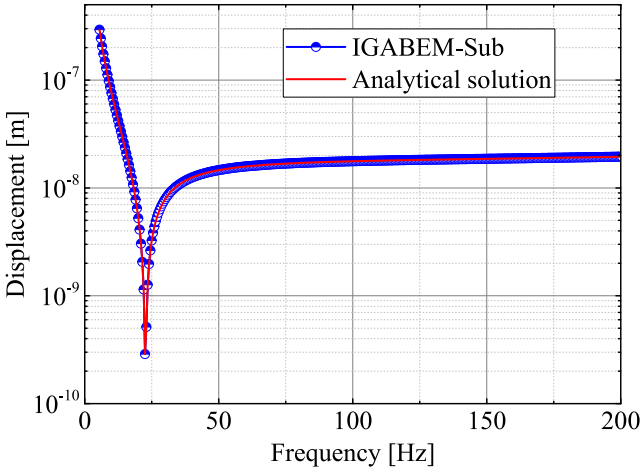

Fig. 9. Comparison between the analytical solutions and numerical results obtained by the IGA-FEM/BEM with subdivision surface for the displacement, calculated at excited point A as function of frequency.

where $\theta_m = m\pi/n$ and $v_f^*(\theta_m) = i\omega u^*(\theta_m)$ with a sufficiently large n.

First, we use subdivision surface method to construct a smooth spherical shell model. Fig. 7 shows the distribution of the initial control points of the spherical shell model. The Catmull–Clark subdivision scheme is used to modify the coordinates of the original geometric control points and insert new control points. The parent quadrilateral mesh is successfully divided into four children elements, and the refinement operation is repeated until the limited smooth surface is obtained. It is worth noting that although the control points and mesh models in each level of subdivision mesh are different, the same surface expression can be obtained after the fitting operation. The fitting surface for every level of subdivision mesh is consistent with the limited surface, similar to the h-refinement property of NURBS.

The spherical shell with subdivision surface is set as the coupling surface for acoustic-structure interaction in this work. It keeps the consistency requirements of the acoustic-structure coupling surface, and avoids the problem that the structure shape changes when the traditional Lagrangian elements are used to encrypt the grid. Therefore, accurate coupling surface can effectively improve the reliability and effectiveness of numerical analysis. Then, we verify the correctness of this algorithm proposed in this work.

The distance between the initial control points and the center point is set as 1. The limited smooth surface constructed by subdivision operation is a smooth spherical surface with a radius of 0.95 m. Herein, the limited surface with 6146 vertices is used for numerical calculation. First of all, we investigate the variation of the amplitude of sound pressure with frequency at the calculated point $2r$ from the spherical center on the x axis in the fluid domain, as shown in Fig. 8. In this figure, "IGABEM-Sub" represents the solution obtained by IGA-FEM/BEM with subdivision surface. By observing the graph, it can be found that the numerical solution is consistent with the analytical solution, which verifies the correctness of the algorithm developed in this work.

Fig. 9 shows that the displacement at the point of action of point force changes with frequency. We can also find that the numerical results are in good agreement with the analytical solutions. In addition, we calculate that the radiated sound power on the structural surface varies with the frequency, as shown in Fig. 10. The radiated sound power reflects the radiated energy of the vibrating structure. If the damping is not considered, the radiated sound power on the closed surface around the structure is the same. We also find that the numerical solution obtained by the algorithm is consistent with the analytical solution. Besides, the relative error between the analytical and numerical solutions of sound pressure at a point $(10, 0, 0)$ is presented in Fig. 11, which proves the correctness of the algorithm. For the last symbol in Fig. 11, the computational time required for solving the structural-acoustic coupling system with 95258 DOFs is 2.1 h.

5.2. Elastic spherical shell

A submersed spherical shell excited by a harmonic force as shown in Fig. 6 is considered in this section. The load excitation point in this

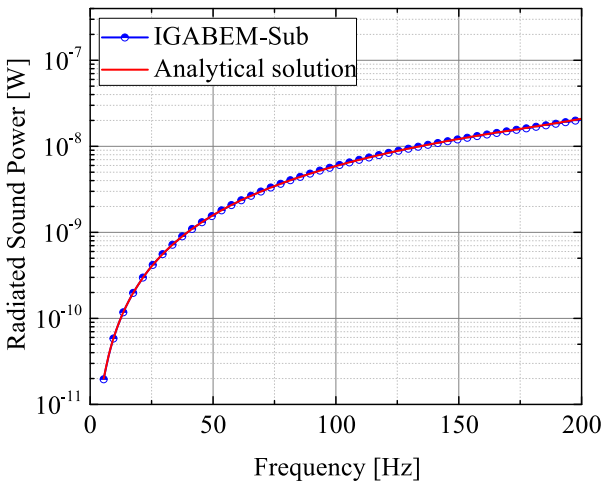

Fig. 10. Comparison between the analytical solutions and numerical results obtained by the IGA-FEM/BEM with subdivision surface for the radiated sound power on the shell structural surface as function of frequency.

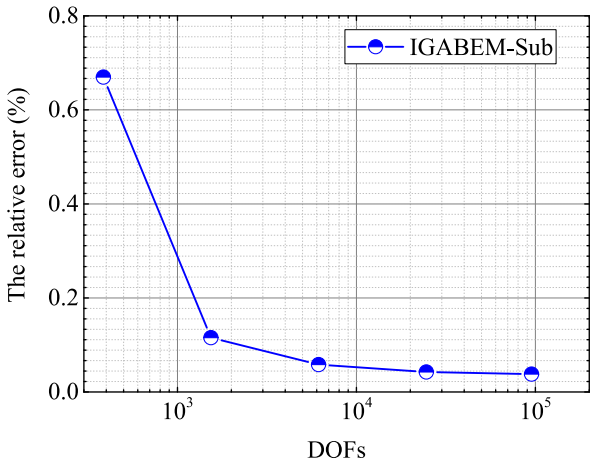

Fig. 11. The relative error between the analytical and numerical solutions of sound pressure at a point $(10, 0, 0)$ with $f = 50$ Hz.

section lies at $(0, 0, r)$ on the z axis. The hemispherical surface with $y < 0$ is set to be design domain. Two kinds of materials will be selected for the design area, namely, steel material and aluminum material. For aluminum material, density $\rho_s = 2100$ kg/m^3, Young's modulus $E = 70$ GPa, and Poisson' ratio $\nu = 0.32$. The remaining hemispherical surface with $y > 0$ is full of steel material.

In the process of material optimization, penalization factor η in Eq. (62) is set as 5, the volume fraction constraint $f_v = 0.5$, and the initial values of design variables are set to be 1. In this work, the sensitivity filter technique with a filter radius of $r_{min} = 0.2$ m is used to suppress the checkerboard patterns and decrease the mesh dependency of the optimization analysis.

Fig. 12 is the convergence plot of objective functions at different frequencies during the optimization process. It can be found that at 200 Hz, the value of the objective function oscillates in the initial stage, and then declines steadily until it converges. Hence, the algorithm developed in this work can effectively reduce sound pressure level and find the corresponding material layout.

The final material layouts obtained by topology optimization at different frequencies are presented in Fig. 13. Purple color represents steel material, and red represents aluminum material. It can be found that the optimization results are frequency dependent, and the material layout at high frequency is more complex. Because of the penalty of material interpolation, a small amount of intermediate densities that are denoted by green units appear at the interface between the red area and the purple area.

After obtaining the optimization results of material distribution at different frequencies, we present the corresponding distribution of sound pressure level on spherical surface, as depicted in Fig. 14. The sound pressure level is represented by the symbol "SPL", which is defined as follows

$$SPL = 20\log_{10}\left[p(e)/p(ref)\right] \tag{69}$$

where $p(e)$ denotes the sound pressure at a computing point, and $p(ref)$ is the reference sound pressure. We also find that the sound pressure level near the excitation is larger than that in other regions, because the larger the displacement and vibration velocity of the excitation point, the larger the sound pressure value is.

5.3. Cube shell

A submersed cube shell excited by a harmonic force as shown in Fig. 15 is considered in this section. The control grid of the geometric model used for numerical solution has 8066 vertices. The approximately rectangular surface with $z > 0.178$ is set to be design domain. Similar to the spherical model above, the design domain is filled by two materials. During the optimization process, the filter radius r_{min} used for sensitivity filter is set to be 0.08 m. The other parameter values are the same as that of the above spherical model.

Fig. 16 is the convergence plot of objective functions at different frequencies during the optimization process. It can be found that the value of the objective function declines steadily until it converges. Hence, the algorithm developed in this work can effectively reduce sound pressure level and find the corresponding material layout.

The optimization results of material distribution at several different frequencies show good symmetry (Fig. 17). A small number of intermediate density elements exist at the interface between the two selected materials, which proves that the algorithm developed in this work is capable of solving practical optimization problems. The frequency dependence of the optimization results is still observable, so it is necessary to develop an optimization analysis method suitable for frequency band instead of the single frequency.

Moreover, the sound pressure distribution over the structural surface corresponding to the optimized material layout at different frequencies is shown in Fig. 18. It can be seen that with the increase of frequency, the optimized sound pressure level exhibits a growing trend, which is particularly manifest for the material layout on the surface portion excited by force.

5.4. Acoustic probe

An acoustic probe model is constructed with Catmull–Clark subdivision surfaces as shown in Fig. 19, which replicates a physical device used for the measurement of acoustic intensity in full-scale rocket motor testing. A similar model built with T-splines was adopted in [41] for acoustic analysis with isogeometric boundary element method. The initial control mesh model for acoustic probe has sharp edges, but the geometric surface constructed from it is smooth. The minimum bounding box of this acoustic probe is defined as $[v_i^{min}, v_i^{max}]^3 = [-1.9, 1] \times [-0.8, 2.2] \times [-1.66, 1.66]$. The thickness of this model is 0.02 m. The control grid of the geometric model obtained after one subdivision has 24768 vertices and is used for numerical solution.

The structure is made of two types of materials and subjected to time harmonic concentrated force. Through optimization analysis, the optimal material layout is obtained to achieve the lowest radiated sound power value. During the optimization process, the filter radius r_{min} used for sensitivity filter is set to be 0.1 m. The volume fraction

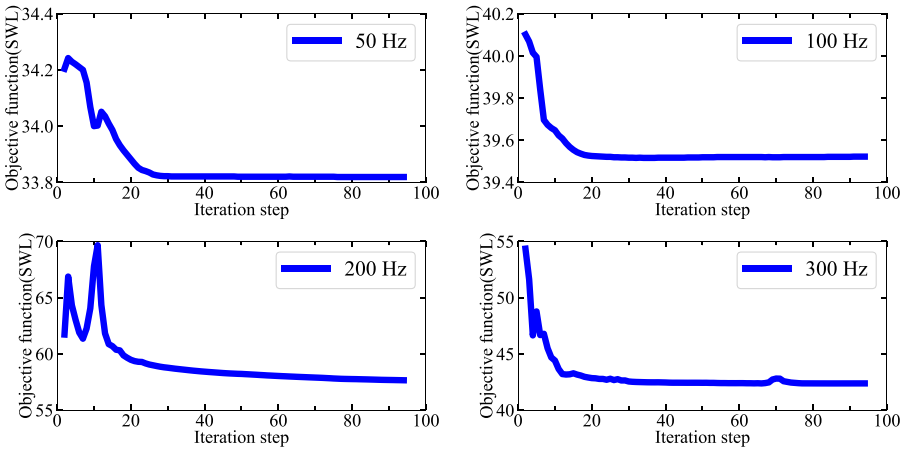

Fig. 12. The convergence of the objective function at different frequencies.

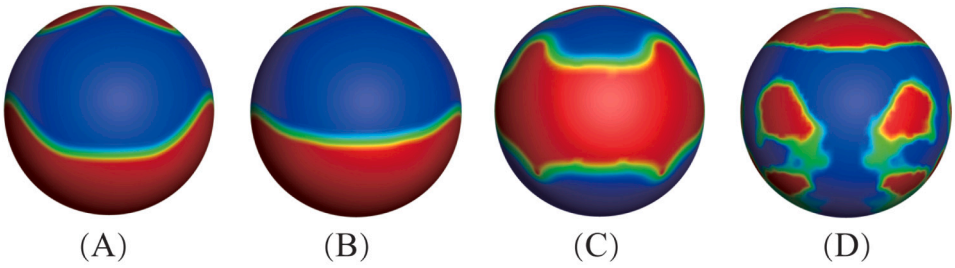

Fig. 13. Topological design of the half-spherical shell at several different frequencies. (A), 50 Hz; (B), 100 Hz; (C), 200 Hz; (D), 300 Hz. (For interpretation of the references to color in this figure legend, the reader is referred to the web version of this article.)

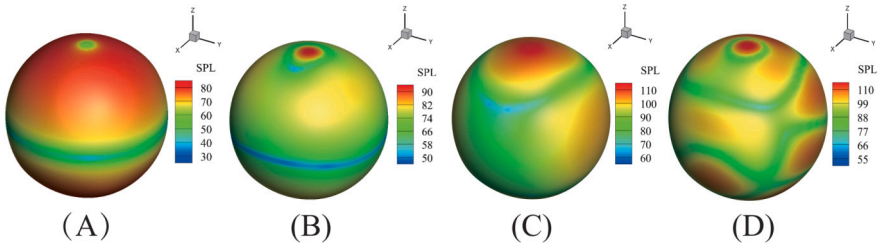

Fig. 14. Sound pressure level on structure surface. (A) 50 Hz; (B) 100 Hz; (C) 200 Hz; (D) 300 Hz.

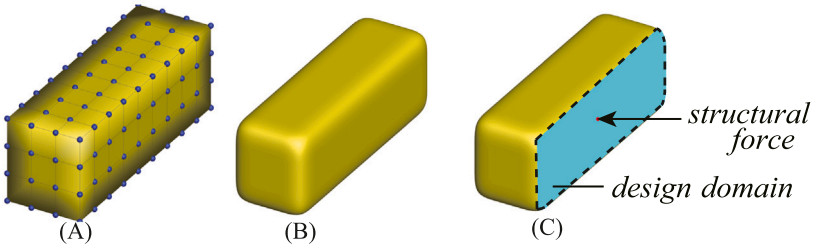

Fig. 15. Cube model setup. (A) the initial coarse subdivision discretization with 128 vertices used to generate control meshes; (B) the limited surface with 8066 vertices. The smoothing effects can be observed in particular at the junction. Subdivision schemes may be applied to manifold meshes, thereby having less restrictions than the spline-based methods; (C) the right surface of cube is selected as design domain and the center point of the surface is the load action point.

constraint is set to be $f_v = 0.5$, and the initial values of the design variables are specified as one. The other parameter values are consistent with that for spherical model.

Fig. 20 is the convergence plot of objective functions at different frequencies during the optimization process. Good convergence is found. This result proves the validity of the algorithm in this paper.

The optimization results of material distribution at several different frequencies are shown in Fig. 21. Herein, four different excitation frequencies, f = 100, 200, 400, and 500 Hz are considered. The sound pressure level distribution on the structural surface with optimized material layout is shown in Fig. 22. The material distributions and sound pressure level layout vary with frequencies, so the optimized results are frequency dependent.

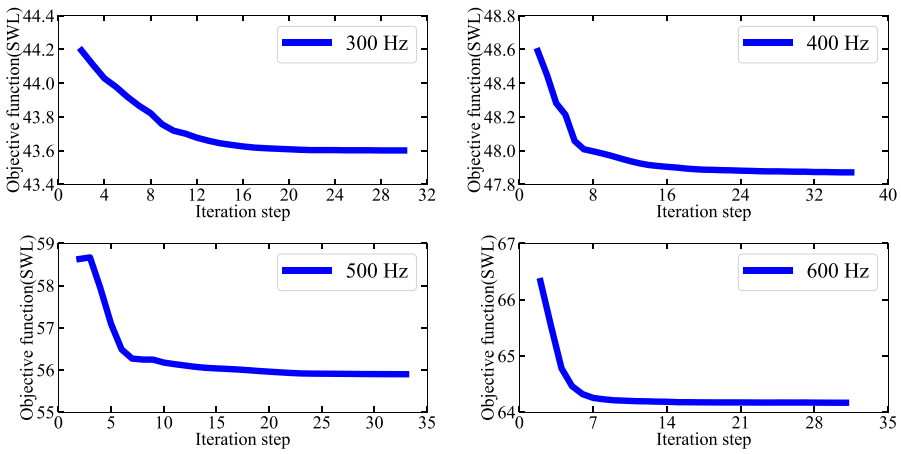

Fig. 16. The convergence of the objective function at different frequencies.

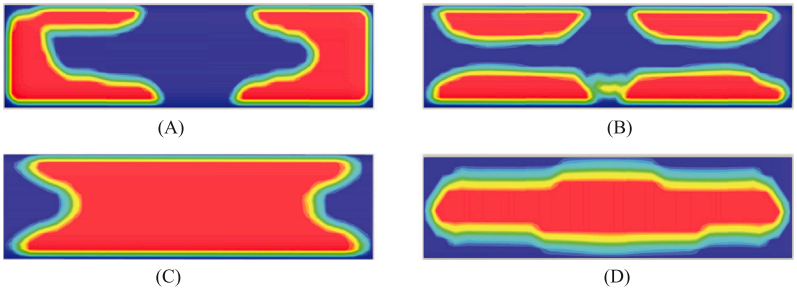

Fig. 17. Topological design of the right surface of cube model at several different frequencies. (A) 300 Hz; (B) 400 Hz; (C) 500 Hz; (D) 600 Hz.

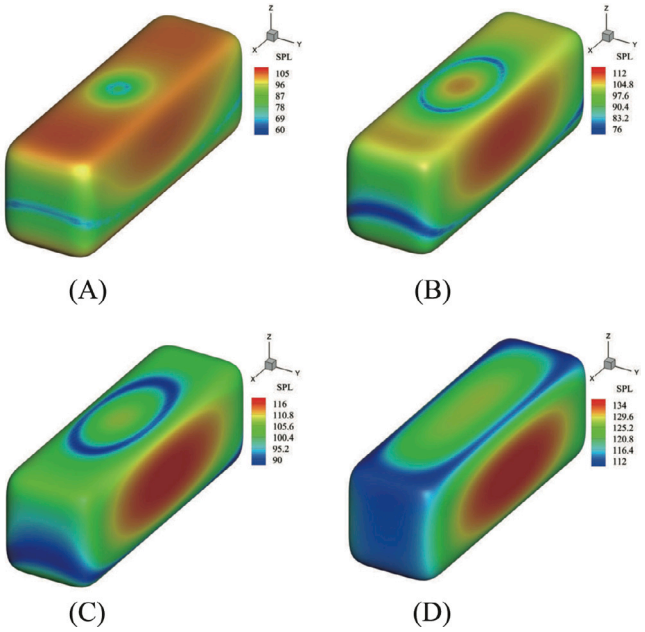

Fig. 18. Sound pressure level on the structure surface. (A) 300 Hz; (B) 400 Hz; (C) 500 Hz; (D) 600 Hz. (Top surface is the design domain).

6. Conclusion

Taking into account the effect of structural-acoustic interaction, we coupled isogeometric FEM and BEM for topology optimization of bimaterial structures. Coupling of the two methods fully exploits their complementary advantages in simulating shell vibration and exterior acoustic problems, respectively. The reasons for introducing isogeometric analysis are threefold: (1) The exactness of geometric models are retained that is crucial to the accuracy of structural-acoustic interaction analysis; (2) High order continuity is achieved that eases the use of

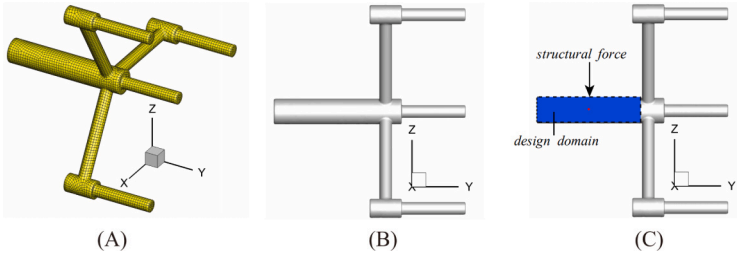

Fig. 19. Acoustic probe model setup. (A), the initial coarse subdivision discretization with 6192 vertices used to generate control meshes; (B), the limited surface with 99072 vertices; (C), selection of design domain and definition of concentrated load.

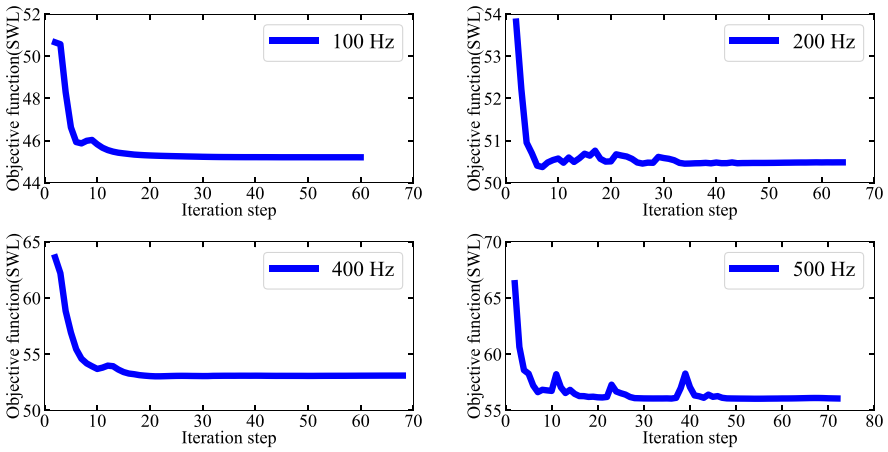

Fig. 20. The convergence of the objective function at different frequencies.

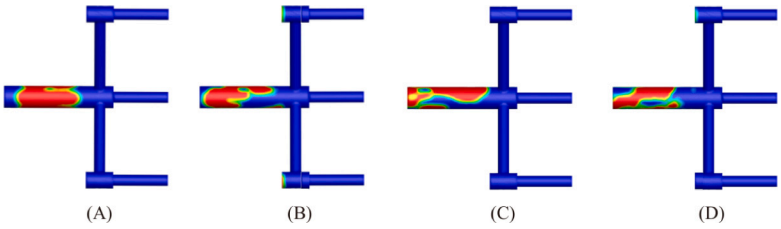

Fig. 21. Topological design of the design surface of acoustic probe model at several different frequencies. (A) 100 Hz; (B) 200 Hz; (C) 400 Hz; (D) 500 Hz.

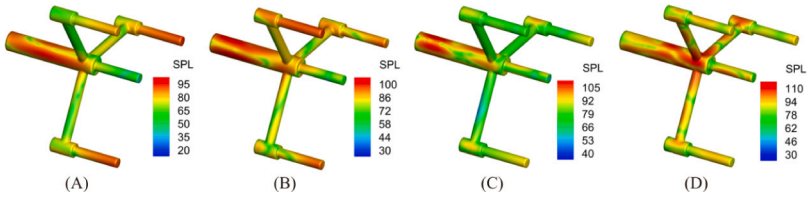

Fig. 22. Sound pressure level on the structure surface. (A) 100 Hz; (B) 200 Hz; (C) 400 Hz; (D) 500 Hz.

Kirchhoff–Love elements; (3) meshing procedures can be eliminated. We adopted Catmull–Clark subdivision surfaces to construct geometric models and discretize physical fields, due to their capability of generating water-tight geometries and tackling extraordinary points. The numerical tests show the superior performance of the present methods in topology optimization for structural-acoustic interaction systems. The examples also indicate that the optimized design is heavily dependent on frequencies. Hence, topology optimization in a frequency band and robust optimization considering frequency variation is of practical significance [58,59]. Furthermore, in our examples all of the geometries are smooth everywhere. In some cases, it is desirable to preserve sharp edges and corners, but it is difficult for the classical subdivision surface method to do that. To overcome this difficulty, extended versions of subdivision surfaces were proposed [60,61], which will be incorporated into our future work.

Acknowledgments

We acknowledge the financial support from National Natural Science Foundation of China (NSFC) under Grant Nos. 51904202, 11702238, and 11872168. S.P.A. BORDAS received funding from the European Union's Horizon 2020 research and innovation programme under grant agreement No 811099 TWINNING Project DRIVEN for the

University of Luxembourg. We also appreciate the support of Luxembourg National Research Fund through the grant "Intuitive modeling and SIMulation platform (IntuiSIM)" (PoC17/12253887).

References

[1] Sigmund O. On the usefulness of non-gradient approaches in topology optimization. Struct Multidiscip Optim 2011;43:589–96.
[2] Zhang X, Kang Z. Topology optimization of damping layers for minimizing sound radiation of shell structures. J Sound Vib 2013;359:183–98.
[3] Du J, Olhoff N. Minimization of sound radiation from vibrating bi-material structures using topology optimization. Struct Multidiscip Optim 2007;33:305–21.
[4] Yoon GH, Jensen JS, Sigmund O. Topology optimization of acoustic–structure interaction problems using a mixed finite element formulation. Internat J Numer Methods Engrg 2007;70:1049–75.
[5] Allaire G, Jouve F, Toader A-M. Structural optimization using sensitivity analysis and a level-set method. J Comput Phys 2004;194(1):363–93.
[6] Ghasemi H, Park H, Rabczuk T. A multi-material level set-based topology optimization of flexoelectric composites. Comput Methods Appl Mech Engrg 2018;332:47–62.
[7] Ghasemi H, Park H, Rabczuk T. A level-set based IGA formulation for topology optimization of flexoelectric materials. Comput Methods Appl Mech Engrg 2017;313:239–58.
[8] Guo X, Zhang W, Zhong W. Doing topology optimization explicitly and geometrically? a new moving morphable components based framework. J Appl Mech 2014;81(8).
[9] Zhang W, Yuan J, Zhang J, Guo X. A new topology optimization approach based on Moving Morphable Components (MMC) and the ersatz material model. Struct Multidiscip Optim 2016;53(6):1243–60.
[10] Christiansen AN, Nobel-Jørgensen M, Aage N, Sigmund O, Bærentzen JA. Topology optimization using an explicit interface representation. Struct Multidiscip Optim 2014;49(3):387–99.
[11] Lian H, Christiansen AN, Tortorelli DA, Sigmund O, Aage N. Combined shape and topology optimization for minimization of maximal von Mises stress. Struct Multidiscip Optim 2017;55(5):1541–57.
[12] Zhou M, Lian H, Sigmund O, Aage N. Shape morphing and topology optimization of fluid channels by explicit boundary tracking. Internat J Numer Methods Fluids 2018;88(6):296–313.
[13] Dühring MB, Jensen JS, Sigmund O. Acoustic design by topology optimization. J Sound Vib 2008;317(3–5):557–75.
[14] Christiansen RE, Sigmund O, Fernandez-Grande E. Experimental validation of a topology optimized acoustic cavity. J Acoust Soc Am 2015;138(6):3470–4.
[15] Cheng A, Cheng D. Heritage and early history of the boundary element method. Eng Anal Bound Elem 2005;29:268–302.
[16] Chen LL, Lu C, Lian H, Liu Z, Zhao W, Li S, et al. Acoustic topology optimization of sound absorbing materials directly from subdivision surfaces with isogeometric boundary element methods. Comput Methods Appl Mech Engrg 2020;362:112806.
[17] Liu Y. On the BEM for acoustic wave problems. Eng Anal Bound Elem 2019;107:53–62.
[18] Xie X, Liu Y. An adaptive model order reduction method for boundary element-based multi-frequency acoustic wave problems. Comput Methods Appl Mech Engrg 2021;373:113532.
[19] Marburg S. Developments in structural-acoustic optimization for passive noise control. Arch Comput Methods Eng 2002;27:291–370.
[20] Marburg S. The Burton and Miller method: Unlocking another mystery of its coupling parameter. J Comput Acoust 2016;23(01):1550016.
[21] Takahashi T, Matsumoto T. An application of fast multipole method to isogeometric boundary element method for Laplace equation in two dimensions. Eng Anal Bound Elem 2012;36(12):1766–75.
[22] Zheng CJ, Bi CX, Zhang C, Gao HF, Chen HB. Free vibration analysis of elastic structures submerged in an infinite or semi-infinite fluid domain by means of a coupled FE–BE solver. J Comput Phys 2018;359:183–98.
[23] Zheng CJ, Gao HF, Du L, Chen HB, Zhang CZ. An accurate and efficient acoustic eigensolver based on a fast multipole BEM and a contour integral method. J Comput Phys 2016;305:677–99.
[24] Liu D, Havranek Z, Marburg S, Peters H, Kessissoglou N. Non-negative intensity and back-calculated non-negative intensity for analysis of directional structure-borne sound. J Acoust Soc Am 2017;142:117–23.
[25] Wilkes DR, Peters H, Croaker P, Marburg S, Duncan AJ, Kessissoglou N. Non-negative intensity for coupled fluid–structure interaction problems using the fast multipole method. J Acoust Soc Am 2017;141:4278–88.
[26] Faugeras B, Heumann H. FEM-BEM coupling methods for tokamak plasma axisymmetric free-boundary equilibrium computations in unbounded domains. J Acoust Soc Am 2017;343:201–16.
[27] Everstine GC, Henderson FM. Coupled finite element/boundary element approach for fluid-structure interaction. J Acoust Soc Am 1990;87(5):1938–47.
[28] Fischer M, Gaul L. Fast BEM–FEM mortar coupling for acoustic–structure interaction. Internat J Numer Methods Engrg 2005;62:1677–90.
[29] Schneider S. FE/FMBE coupling to model fluid–structure interaction. Internat J Numer Methods Engrg 2008;76:2137–56.
[30] Legay A. An extended finite element method approach for structural-acoustic problems involving immersed structures at arbitrary positions. Internat J Numer Methods Engrg 2013;93(4):376–99.
[31] Legay A. The extended finite element method combined with a modal synthesis approach for vibro-acoustic problems. Internat J Numer Methods Engrg 2015;101(5):329–50.
[32] Hughes TJR, Cottrell JA, Bazilevs Y. Isogeometric analysis: CAD, finite elements, NURBS, exact geometry and mesh refinement. Comput Methods Appl Mech Engrg 2005;194:4135–95.
[33] Simpson RN, Liu Z, Vazquez R, Evans JA. An isogeometric boundary element method for electromagnetic scattering with compatible B-spline discretizations. J Comput Phys 2018;362:264–89.
[34] Gong Y, Dong C. An isogeometric boundary element method using adaptive integral method for 3D potential problems. J Comput Appl Math 2017;319:141–58.
[35] Wang Y, Benson DJ, Nagy AP. A multi-patch nonsingular isogeometric boundary element method using trimmed elements. Comput Mech 2015;56(1):173–91.
[36] Marussig B, Hughes TJR. A review of trimming in isogeometric analysis: challenges, data exchange and simulation aspects. Arch Comput Methods Eng 2018;25(4):1059–127.
[37] Bazilevs Y, Calo VM, Cottrell JA, Evans JA, Hughes TJR, Lipton S, et al. Isogeometric analysis using T-splines. Comput Methods Appl Mech Engrg 2010;199(5–8):229–63.
[38] Cirak F, Ortiz M, Schröder P. Subdivision surfaces: a new paradigm for thin-shell finite-element analysis. Internat J Numer Methods Engrg 2000;47:2039–72.
[39] Bandara K, Cirak F, Of G, Steinbach O, Zapletal J. Boundary element based multiresolution shape optimisation in electrostatics. J Comput Phys 2015;297:584–98. http://dx.doi.org/10.1016/j.jcp.2015.05.017.
[40] Li J, Dault D, Liu B, Tong Y, Shanker B. Subdivision based isogeometric analysis technique for electric field integral equations for simply connected structures. J Comput Phys 2016;319:145–62.
[41] Simpson RN, Scott MA, Taus M, Thomas DC, Lian H. Acoustic isogeometric boundary element analysis. Comput Methods Appl Mech Engrg 2014;269:265–90.
[42] Liu Z, Majeed M, Cirak F, Simpson RN. Isogeometric FEM-BEM coupled structural-acoustic analysis of shells using subdivision surfaces. Internat J Numer Methods Engrg 2018;113:1507–30.
[43] Yang H, Dong C, Wu Y, Dai R. Mixed dimensional isogeometric FE-BE coupling analysis for solid–shell structures. Comput Methods Appl Mech Engrg 2021;382:113841.
[44] Chen LL, Liu C, Zhao W, Liu L. An isogeometric approach of two dimensional acoustic design sensitivity analysis and topology optimization analysis for absorbing material distribution. Comput Methods Appl Mech Engrg 2018;336:507–32.
[45] Chen LL, Lian H, Liu Z, Chen H, Atroshchenko E, Bordas S. Structural shape optimization of three dimensional acoustic problems with isogeometric boundary element methods. Comput Methods Appl Mech Engrg 2019;355:926–51.
[46] Shaaban A, Anitescu C, Atroshchenko E, Rabczuk T. 3D isogeometric boundary element analysis and structural shape optimization for Helmholtz acoustic scattering problems. Comput Methods Appl Mech Engrg 2021;384(2):113950.
[47] Catmull E, Clark J. Recursively generated B-spline surfaces on arbitrary topological meshes. Comput Aided Des 1978;10(6):350–5.
[48] Stam J. Exact evaluation of Catmull-Clark subdivision surfaces at arbitrary parameter values. In: Siggraph. vol. 98, Citeseer; 1998, p. 395–404.
[49] Doo D, Sabin MA. Behaviour of recursive division surfaces near extraordinary points. Comput Aided Des 1978;10:356–60.
[50] Burton AJ, Miller GF. The application of integral equation methods to the numerical solution of some exterior boundary-value problems. Proc R Soc A 1971;323(1553):201–10. http://dx.doi.org/10.1098/rspa.1971.0097.
[51] Guiggiani M. A self-adaptive co-ordinate transformation for efficient numerical evaluation of general boundary element integrals. Internat J Numer Methods Engrg 1988;26(7):1683–4.
[52] Gao XW, Yang K, Wang J. An adaptive element subdivision technique for evaluation of various 2D singular boundary integrals. Eng Anal Bound Elem 2008;32:692–6.
[53] Rong J, Wen L, Xiao J. Efficiency improvement of the polar coordinate transformation for evaluating BEM singular integrals on curved elements. Eng Anal Bound Elem 2014;38(jan.):83–93.
[54] Zhou F, You Y, Li G, Xie G. The precise integration method for semi-discretized equation in the dual reciprocity method to solve three-dimensional transient heat conduction problems. Eng Anal Bound Elem 2018;95:160–6.
[55] Zhou F, Wang W, Xie G, Liao H, Cao Y. The Distance-Sinh combined transformation for near-singularity cancelation based on the generalized Duffy normalization. Eng Anal Bound Elem 2019;108:108–14.
[56] Chen LL, Zhang Y, Lian H, Atroshchenko E, Bordas SPA. Seamless integration of computer-aided geometric modeling and acoustic simulation: Isogeometric boundary element methods based on Catmull-Clark subdivision surfaces. Adv Eng Softw 2020;149:102879.

[57] Svanberg K. The method of moving asymptotes—a new method for structural optimization. Internat J Numer Methods Engrg 1987;24:359–73.
[58] Wang F, Jensen JS, Sigmund O. Robust topology optimization of photonic crystal waveguides with tailored dispersion properties. Opt Soc Am 2011;28:387–97.
[59] Lazarov BS, Wang F, Sigmund O. Length scale and manufacturability in density-based topology optimization. Arch Appl Mech 2016;86:189–218.
[60] Ying L, Zorin D. Nonmanifold subdivision. In: Proceedings Visualization, 2001. IEEE; 2001, p. 325–569.
[61] Biermann Henning, Levin Adi, Zorin Denis. Piecewise smooth subdivision surfaces with normal control. In: Proceedings of the 27th annual conference on computer graphics and interactive techniques. 2000, p. 113–20.